Chapter 19
Rheology-Based Techniques

Braulio Macias-Rodriguez

Abbreviations

LAOS   Large amplitude oscillatory shear
LVR   Linear viscoelastic region
SAOS   Small amplitude oscillatory shear

19.1   Introduction

"Rheology" is a branch of physics concerned with deformation and flow behavior experienced by complex fluids or soft materials such as foods, when acted on by forces. Such forces may be "naturally" exerted or deliberately applied during processing, use, and consumption. For example, at equilibrium, the fat microstructure is held by van der Waals-London forces, whereas under dynamic conditions, the microscopic ensemble is dictated by shear causing plastic flow. Rheological properties are also related to the application, use, and sensorial properties of fats and encode the effects of formulation and processing imposed on the fat microstructure. These insights in turn are used to establish rheology-structure models linking shear modulus and microstructure, rheology-texture relationships such as describing firmness in terms of shear compliance, and rheology-formulation-processing relationships such as describing the effect of molecular composition, shear/cooling fields on firmness. All these aspects are of paramount importance in designing alternative lipid-structuring systems.

B. Macias-Rodriguez (✉)
Deparment of Food Science and Human Nutrition, University of Illinois Urbana-Champaign, Urbana, IL, USA

In this chapter, I touch upon the abovementioned aspects, but focusing largely on the rheological and mechanical characterization of lipid-based materials, also applicable to oleogels. It is important to highlight that rheological and mechanical properties are material properties intimately related to textural attributes. While in some cases, it is possible to draw clear relationships among them; in some other cases, rheological measurements need to be supplemented by textural measurements. Part of this challenge arises due to the highly heterogenous and multiscale structure of lipids and the complexity of texture as a multisensorial property [1]. I briefly describe the foundations of the main methods to measure rheological, mechanical properties, and textural attributes, and detail the underlying equations describing such measures. A larger section is devoted to large amplitude oscillatory shear. Finally, experimental caveats and study cases relevant to lipid-based materials and oleogels are also provided.

## 19.2 Rheological and Textural Methods

19.2.1 Empirical Methods

19.2.1.1 Penetrometry

Penetrometry has been by far the most popular methods to evaluate the texture of edible fats. This method offers simple and inexpensive characterization which is useful for investigating the effect of processing conditions on consistency and making correlations with sensory panels. The method is based on the resistance of a material to be penetrated or indented by a test body: rod, cone, sphere, needle, etc. The resistance is measured as load, depths, or rates of indentation/penetration of the testing body. To date, cones remain the most common geometries to measure consistency [2]. A schematic representation of a typical cone is shown in Fig. 19.1.

Conical configurations varying in loads and angles cover a range of textures. Most studies include constant load experiments or to a less extent constant rate experiments, both of which show good agreement with one another [4, 5]. The general rule for cone angle selection is the harder (more solid) the material, the smaller the cone angle should be. The most common methods include the AOCS method Cc16-60 and the method proposed by Haighton [4]. Results are reported as penetration depths or converted into yield values, hardness, or spreadability indexes, using various equations dependent on the testing body and test conditions [4]. Considering that most of the force is used to overcome the yield point, the stress at which deformations are a combination of elastic "reversible" and plastic "irreversible" deformations, and provided that the motion is slow, an empirical yield value C is defined as the force load per unit cross-sectional area of the cone as given by,

$$C = \frac{K'W}{p^n} \tag{19.1}$$

Fig. 19.1 Schematic representation of a conical probe. Applied force F, cone radius r, arbitrary penetration height h. (Reproduced from [3], with permission from Springer Nature)
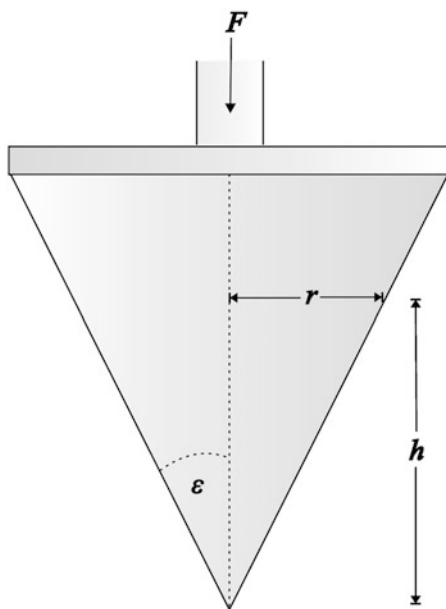
Table 19.1 Examples for yield point values for margarine [4]

C-values		
<100	200–800	>1500
Very soft, not shape retaining	Best consistency, easy to spread	Too hard, no more spreadable

where K' is a constant dependent on the cone angle, W is the weight of the cone (g), p is the penetration depth raised to a fractional power $1.4 \leq n \leq 2$ as found empirically. The values of these empirical coefficients appear to depend on hardness and type of fat [4, 6] suggesting a complex relationship between the cone and yield value (e.g., for butter $n \approx 1.6$). The yield value may be affected by frictional forces between the fat and the tested material, though these are negligible for truncated cones [2]. Table 19.1 shows exemplary C values calculated according to Eq. 19.1 to help classify the consistency of margarine:

Additional definitions of apparent yield stress, hardness, and spreadability have been proposed [2]. Despite the advantage of cone penetrometry, some of the main arguments made against its use include poor reproducibility for firm butters, use of arbitrary testing conditions (e.g., penetration time), and ill-defined measures of yield value [2]. These assertions are supported by studies reporting the inability of cone penetrometry to differentiate among textural attributes of butter, limited degree of correlation of yield values with spreadability, and lack of universal material measures [4, 7, 8].

19.3 Fundamental Methods

19.3.1 Pressure-Driven Flow: Capillary Rheometry

Capillary or orifice die extrusion flows are useful for determining viscosities and yield stress of viscoplastic fluids such as edible fats under controlled extrusion-like processes [9, 10]. For this, a capillary rheometer is used which consists of a driving a tool namely a piston or ram, moving at a linear speed v to force material through a barrel with radius D_B and a die of radius D and length L (Fig. 19.2) [11].

From the pressure signal, the apparent die wall shear stress σ_w^{app} is calculated according to the following equation:

$$\sigma_w^{app} = \frac{\Delta P_{tot}}{2} \frac{R}{L} \tag{19.2}$$

where ΔP_{tot} is the total pressure drop with respect to the die exit, R is the die radius, and L is the die length. Apparent die wall shear rates $\dot{\gamma}_w^{app}$ are related to ram velocities v according to:

$$v = \frac{\dot{\gamma}_w^{app} R^3}{4 R_B^2} \tag{19.3}$$

Fig. 19.2 Schematic view of a material being extruded through an orifice die with diameter D and length L in a capillary rheometer. Pressure P is applied by a piston with velocity v and measured by a manometer during the test. (Reproduced from [3], with permission from Springer Nature)
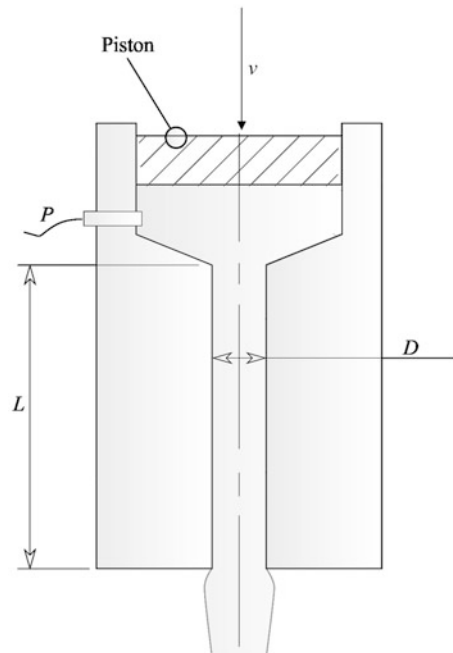
where R^3 is the die radius and R_B^2 is the barrel radius. To interpret the results in terms of true material measures, corrections including Bagley, Mooney, and Weissenberg-Rabinowitsch to account for entrance pressure losses due to contractional flow, wall slip, and non-Newtonian flow profile must be applied, respectively.

Bagley Correction
The overall pressure loss ΔP_{tot} for fluid flow through a die may be expressed as:

$$\Delta P_{\text{tot}} = \Delta P_{\text{visc}} + \Delta P_{\text{Bag}} \qquad (19.4)$$

where ΔP_{visc} is the viscous pressure drop in the die and ΔP_{Bag} the entrance flow pressure drop component, called Bagley pressure. The Bagley correction consists in obtaining pressures drops at least at two shear rates using capillaries with the same D but varying lengths L ratios and extrapolation to a die of zero length. The true die wall shear stress can be calculated as follows:

$$\sigma_w = \frac{\Delta P_{\text{tot}} - \Delta P_{\text{Bag}}}{2} \frac{R}{L} \qquad (19.5)$$

Mooney Correction
From the expression of the apparent die wall shear rate $\dot{\gamma}_w^{\text{app}}$:

$$\dot{\gamma}_w^{\text{app}} = \frac{4\dot{Q}}{\pi R^3} = \frac{4v}{R} \qquad (19.6)$$

We can decompose the velocity into the sum of the slip v_{slip} and true v_{true} velocity contributions:

$$\dot{\gamma}_w^{\text{app}} = \frac{4v}{R} = \frac{1}{R}\left(4v_{\text{true}} + 4v_{\text{slip}}\right) = \dot{\gamma}_w + \frac{4v_{\text{slip}}}{R} \qquad (19.7)$$

The slope of the apparent die wall shear rate as function of the reciprocal radius $1/R$ for a given die wall shear stress yields $4v_{\text{slip}}$. The slip contribution is determined using a set of dies with the same L/D but different diameters D. Equation 19.7 is used to estimate the wall slip velocity, which then is fitted to a discrete function such as a power-law or polynomial based on a best-fit approach, and then the wall shear rate for Newtonian fluids $\dot{\gamma}_w$ is obtained.

Weissenberg-Rabinowitsch Correction
The true non-Newtonian die shear rate $\dot{\gamma}$ can be expressed as:

$$\dot{\gamma} = \dot{\gamma}_w\left[\frac{1}{4}\left(3 + \frac{d\ln\dot{\gamma}_w}{d\ln\sigma_w}\right)\right] \qquad (19.8)$$

The dependency of $\ln(\dot{\gamma}_w) = f(\ln(\sigma_w))$ may not always be linear. Therefore, higher-degree polynomial functions are fitted onto the data to yield a continuously differentiable function. Then, the first derivative of the fitted polynomial function can be used to calculate the true non-Newtonian die shear rate $\dot{\gamma}$.

Using the stress σ_w and the corrected non-Newtonian shear rate $\dot{\gamma}_w$ at the wall, the shear viscosity η can be estimated:

$$\eta = \frac{\sigma_w}{\dot{\gamma}_w} \tag{19.9}$$

The entrance pressure can also be used to estimate the extensional viscosity μ. Pressure drops can also be utilized to calculate the yield stress [9]. Considering constant volume, zero length orifice die, plastic behavior, and rate dependence of pressure, the following relationship has been proposed:

$$P = 2(\sigma_0 + \alpha V^n) \ln \frac{D_0}{D} \tag{19.10}$$

where P denotes the pressure to deform a material from its original diameter D_0 to a final diameter D, σ_0, α, and n can be considered material constants independent of die geometry and extrusion rate. The extensional yield stress σ_0 can be converted into a shear stress according to Von Mises yield criterion,

$$\sigma_0 = \frac{\sigma_y}{\sqrt{3}} \tag{19.11}$$

Castro et al. [9] recently applied this method to the characterization of the yield stress of soft solids and found good correlation with results obtained from rotational steady shear measurements.

19.3.2 Compression

Compression tests are one of the most popular tests for determining fundamental rheological, fracture properties, and empirical textural attributes due to their practicability and easiness of interpretation (Fig. 19.3). Compression tests consist in deforming a specimen of known dimensions such as a cylinder at constant force (creep) or at constant crosshead speed (axial compression) for a determined time.

For creep compression, deformation is measured as a function of time, whereas for axial compression, force is recorded as a function of time. Most literature involves uniaxial compression, in which, force-time curves are converted into

Fig. 19.3 Schematic illustration of a soft material being compressed at constant speed rate. Stress-strain curves depict linear and nonlinear regimes from which an apparent elastic modulus, yield stress, and strain can be determined
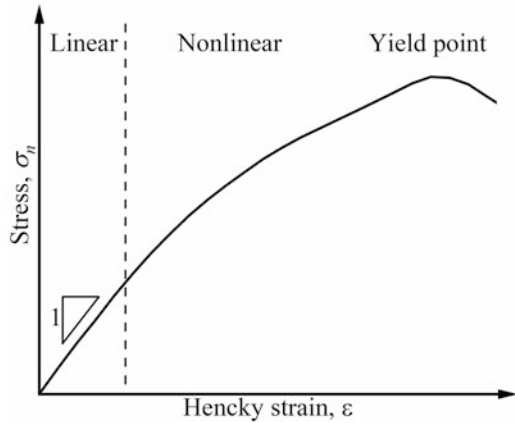
normal stress σ_n versus Hencky strain ε or strain rate $\dot{\varepsilon}$ curves. Treating fats and oleogels as incompressible materials, σ_n, ε and $\dot{\varepsilon}$ can be calculated as follows [12]:

$$\sigma_n = \frac{F}{A} \tag{19.12}$$

$$\varepsilon = \ln\left(\frac{h_t}{h_0}\right) \tag{19.13}$$

$$\dot{\varepsilon} = \left(\frac{d\varepsilon}{dt}\right) = \frac{\dot{h}}{h} \tag{19.14}$$

where A is the circular area of a cylinder with diameter D, h_0, and h_t are the specimen heights at the beginning and during the test. From the uniaxial compression curves, apparent rheological measures including the Young's modulus E_{app}, the yield point σ_{y_app}, and the viscosity η_{app} can be calculated. The E_{app} is measured as the first derivative $d\sigma_n/d\varepsilon$ of the beginning of the compression curve where $\varepsilon \to 0$, the σ_{y_app} is defined as the maximum stress and the η_{app} is determined from the slope $d\sigma_n/d\dot{\varepsilon}$. Some limitations of compressive test include their limited range of accuracy since a true elastic modulus cannot be measured for yield strains below ~1% which is within the yielding region of edible fats and oleogels, manifestation of cracks or strain localization due to large strains, buckling or bulging of the sample specimens, and strong frictional effects at the boundary of the sample. Adequate specimen sizes $h_0/D \sim 1{-}1.5$ and lubricated plates (e.g., coated with oil or Teflon) can be used to circumvent the last two effects [12].

19.3.3   Drag Flow: Shear Rheology

Shear rheometry can be performed under rotational or oscillatory modes. The rotational mode, consisting of a steady shear input, enables the determination of compliance, shear-thinning flow behavior, and time dependence. The oscillatory mode comprises periodic shear inputs made of small or large strains or stresses at fixed or varying frequency.

19.3.3.1   Steady Shear Flow

Steady shear flow measurements are useful to determine the static or dynamic yield stress σ_y, depending on how the shear-rate ramps are performed, and shear-thinning behavior (Fig. 19.4a). "Slurry type" samples having a $\sigma_y \lesssim 10^0$–10^2 Pa are more adequate for steady-shear rates than stiffer samples, which are more prone to flow instabilities such as edge fracture, slip. When conducting steady-shear flow experiments, dependence on gap size can indicate confined flow. For the global flow behavior, the data can be described by the Herschel-Bulkley model:

$$\sigma = \sigma_y + K\dot{\gamma}^n \tag{19.15}$$

where σ_y denotes the dynamic or static yield stress for descending or ascending shear, respectively, K is a proportionality constant, and n is a power law index.

19.3.3.2   Step Shear: Creep and Recovery

Creep and recovery tests consist in applying a step stress input $\sigma(t) = \sigma_0 H(t)$, where $H(t)$ is a Heaviside step function and following the evolution of the strain $\gamma(t)$ in the material over time, to obtain the compliance $J(t) \equiv \gamma(t)/\sigma_0$ (Fig. 19.4). Based on these
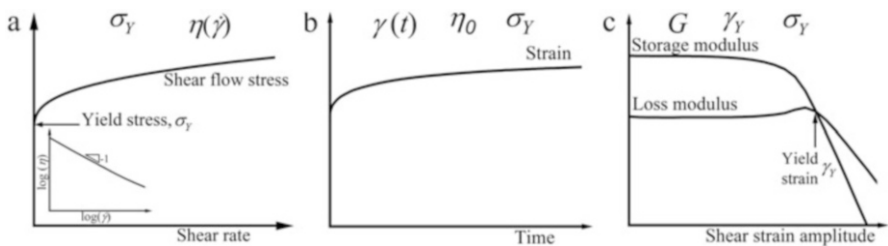
Fig. 19.4 Schematic illustration of different shear modes: (**a**) steady shear, (**b**) step shear: creep phase, and (**c**) oscillatory shear. Key rheological properties are also depicted, including (**a**) yield and viscosity from a steady shear test, (**b**) strain, zero-shear viscosity, and yield stress from a step shear creep experiment, and (**c**) viscoelastic moduli, yield strain, and yield stress from an oscillatory amplitude shear experiment

material measures, rheological definitions for textural attributes such as firmness, springiness, and rubberiness have been proposed for lipid-filled gels such as cheese.

Firmness

Firmness can be judged while deforming a piece of cheese with the mouth (tongue and palate, incisors, front teeth or molars) or by hand. Past studies suggest that firmness is a linear viscoelastic property. Instrumentally, it can be defined as a resistance to creep, and can be expressed by the inverse of the maximum compliance $J(t)$ measured at the end of the creep phase. The time at which a texture attribute is measured is called the time of observation. For firmness, this time is denoted as t_f. Thus, firmness F is mathematically defined as:

$$F \equiv \frac{1}{\max\{J(t)\}} = \frac{1}{J(t_f)} \tag{19.16}$$

and has units of Pa.

Springiness

Springiness deals with sudden responses that are evaluated over a short period of time and thus the use of a rate is appropriate. Springiness is defined as the absolute secant rate of recovery just after the stress is released and is judged at a time of observation $t_s = t_f + \triangle t_s$. Thus, springiness S is mathematically defined as:

$$S \equiv \frac{\left|J(t_s) - J(t_f)\right|}{t_s - t_f} = \frac{\left|J(t_f + \Delta t_s) - J(t_f)\right|}{\Delta t_s} \tag{19.17}$$

and has units of $(\text{Pa s})^{-1}$, which is equal to the inverse of the units of viscosity. In practice one judges S of a material such as cheese, by observing the instantaneous response when the stress releases. It is thus logical to take $\triangle t_s \ll t_f$, which is the minimum response time of modern rheometers $\triangle t_s = 0.1$ s.

Rubberiness

Rubberiness is related to the extent of strain recovery during a measurement time interval (t_f, t_r), where t_r is the time for measuring rubberiness R. If the strain is fully recovered at the time $t = t_r$, then $R = 1$. If there is no strain recovery at $t = t_r$, then $R = 0$. Thus, rubberiness is mathematically defined as:

$$R \equiv \frac{J(t_f) - J(t_r)}{J(t_f)} = 1 - \frac{J(t_f + \Delta t_r)}{J(t_f)} = 1 - F(t_f)J(t_f + \Delta t_r) \tag{19.18}$$

which is a dimensionless quantity, where $\triangle t_r$ is the elapsed time of recovery for measuring rubberiness. Similar measures of F and R were proposed based on oscillatory measures of the complex modulus G^*, frequency ω_f, and the yield strain amplitude γ_0.

The time dependence of creep tests makes them particularly suitable for evaluating mechanical responses both for short time (material compliance and firmness) and for long times (such as creeping of stacked butter in store). The load and the duration of the time should be high and long enough, respectively, to induce sufficient creep motion but not too high or long to trigger formation of cracks [13].

Another use of creep tests is for the determination of the yield stress σ_y, where for $\sigma_0 < \sigma_y$ results in $\gamma(t)$ curves characterized by an increase in strain and then a plateau or saturation (a hallmark of the solid regime of pastes), and $\sigma_0 > \sigma_y$ the same curves tend to a straight line with slope 1 in logarithmic scale, indicating infinite deformation at constant rate (a hallmark of the liquid regime of pastes) [14]. Experimentally, for stresses $\sigma_0 < \sigma_y$, creep compliance curves overlap or nearly overlap onto each other, whereas for stresses $\sigma_0 > \sigma_y$, deviations from this behavior occur and indicate the onset of nonlinear behavior. However, calculation of σ_y by this method may prove inefficient and unfeasible in stiff pastes due to heterogenous flow imposed by sudden stress jumps and higher sensitivity of this method to structural changes over long periods at constant stress [15].

19.3.3.3   Oscillatory Shear

During oscillation, a sinusoidal input function (strain or stress) is applied, and the associated response is measured (Fig. 19.4). The response comprises in-phase (stored energy or elastic modulus) and out-of-phase (loss energy or loss modulus) components with respect to the input function. Depending on the amplitude of the input function, oscillatory shear can be divided into two main regimes: small amplitude and large amplitude, which probe linear and nonlinear viscoelastic regions, respectively. Compared to other fundamental tests, oscillatory shear allows simultaneous characterization of elastic and viscous properties in a broad spectrum of flow conditions.

Small Amplitude Oscillatory Shear (SAOS)
Small amplitude oscillatory shear (SAOS) tests are useful to measure viscoelastic properties of the underlying microstructure. SAOS imposes relatively small strains or stresses in the linear viscoelastic region (LVR) typical of materials interacting via short-range van der Waals forces such as lipids and oleogels [16]. During SAOS tests, strain and stress maintain their linear proportionality and the crystal network exhibits viscoelastic solid-like behavior ($G' > G''$) characterized by high moduli G', $G'' \approx 10^4$–10^6 Pa, and weak frequency (ω) dependence [16–18]. For a sinusoidal strain excitation $\gamma(t) = \gamma_0 \sin(\omega t)$, a sinusoidal stress response $s(t) = g_0 \sin(\omega t + \delta)$ is obtained at the same input frequency ω, and with phase angle δ. The response can be decomposed as

$$s(t) = \gamma_0 G'(\omega) \sin(\omega t) + \gamma_0 G''(\omega) \cos(\omega t) \tag{19.19}$$

In which G', the in-phase elastic modulus or stored energy represents the real component, and G'', the out-of-phase viscous modulus or dissipated energy represents the imaginary component of the complex modulus $G^*(\omega) = G'(\omega) + iG''(\omega)$ at a given frequency ω [11]. Linear viscoelastic properties are useful for developing the structure-property relations such as linking interaction forces holding a network to its linear moduli. The magnitude of the elastic modulus G' of fats depends in a complex manner on at least three factors: volume fraction (SFC/100), crystal microstructure, and crystalline interactions [17]. The elastic modulus G' and G'' provides a combined measure of primary crystallization, aggregation, and network formation, as well as of material hardness or firmness [17]. A Fourier analysis, which converts the time function into frequency domain, of the stress response reveals in the LVR region that only the first or fundamental harmonic ($n = 1$) associated with ω occurs.

Large Amplitude Oscillatory Shear (SAOS)

The LAOS regime occurs above a yielding strain or stress, where materials plastically deform, and their response is no longer sinusoidal. The yield stress σ_y is an important property linked to sensory attributes such as spreadability. From oscillatory experiments, σ_y can be defined in several ways namely the stress: (i) at which the elastic G' starts to decay by certain percentage, (ii) where power-law fits of stress-strain curves intersect, and (iii) where G' and G'' crossover. The first two methods give the lowest estimates of σ_y and γ_y, whereas the latter provides the highest values of σ_y and γ_y since the material experiences substantial yielding. For fats and oleogels, the onset of nonlinear behavior occurs at $\gamma_y \approx 0.1\%$. There are several approaches to interpret the nonlinear LAOS data, including examining the behavior of the first-harmonic moduli, time-domain stress waveforms $\sigma(t)$ or two-coordinate axes figures referred as to Lissajous-Bowditch curves, and analyzing the raw waveforms via FT rheology, Chebyshev stress decomposition, sequence of physical processes, etc. [19, 20]. The first-harmonic or average viscoelastic moduli G' and G'' denote the global ("full" or "intercycle") stress response. Figure 19.3 shows an example of a typical edible fat: butter. The material undergoes average elastic softening coupled with increase dissipation or thinning due to disruption of the crystal network as strain increases. Time-domain raw signals $\sigma(t)$ and Lissajous-Bowditch curves qualitatively distinguish among material response and capture the onset of nonlinear behavior. Lissajous-Bowditch curves are closed loop plots of γ_0 on the abscissa and $\sigma(t)$ on the ordinate (elastic representation) or $\dot{\gamma}_0$ on the abscissa and $\sigma(t)$ on the ordinate (viscous representation). Figure 19.5 shows raw elastic Lissajous-Bowditch plots of butter within and outside the LVR for butter at $T = 18\,°C$.

Within the LVR region ($\gamma_0 < 0.01\%$), the plots mirror nearly "perfect" ellipses, where the tangent slope corresponds to G' and the area enclosed by the ellipse represents G''. Beyond amplitudes where yielding begins ($\gamma_0 > 0.01\%$), the plots become gradually distorted and acquire square-like shapes enclosing increasingly larger areas [19]. Typical features, e.g., global strain softening, and additional local features, e.g., intracycle stiffening, masked by the average viscoelastic moduli can be
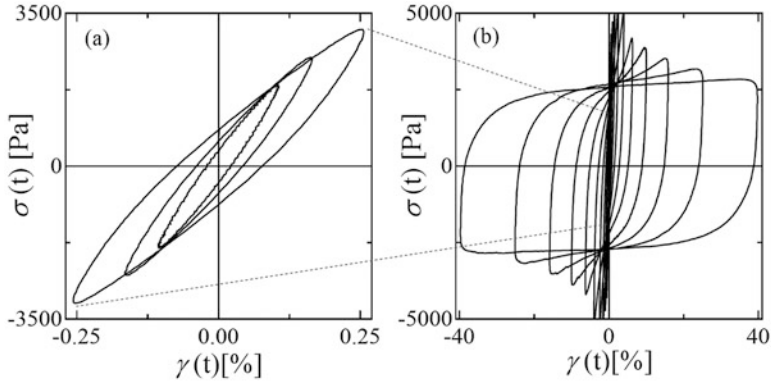
Fig. 19.5 Raw Lissajous-Bowditch plots (elastic perspective) of butter ($T = 18$ °C) obtained from an oscillatory shear test ($\omega = 3.6$ rad/s) (**a**) linear to mildly nonlinear transition (SAOS to LAOS), (**b**) fully nonlinear response (LAOS). (Reproduced from [3], with permission from Springer Nature)

visualized. Global or average elastic softening is manifested as intercycle clockwise rotation in the slope of the stress-strain curve at strain minima $\gamma_0 = 0$ (i.e., at the "origin" where strain rate $\dot{\gamma}$ is at maxima) toward the strain-axis. Local strain stiffening is clearly visible as the intracycle upturn of the shear stress at strain maxima $\gamma_0 = $ max (i.e., at the "extreme" where $\dot{\gamma} = 0$). Stress overshoots, akin to those observed during a start-up shear test, appear in the upper left quadrant of the Lissajous-Bowditch and indicate yielding. The reversibility of the observed behavior during flow reversal evokes microstructure "healing" or thixotropy [21]. While the first-harmonic viscoelastic moduli are the common output of most rheometers, locally defined measures are calculated using frameworks developed to analyze the nonlinear response such as FT, Chebyshev stress decomposition method, and sequence of physical processes. The FT analysis converts time-domain periodic signals into frequency-domain signals that make up a spectrum encompassing first and higher-order odd harmonics ($n = 1, 3, 5\ldots$) in the case of nonlinear response. Despite the quantitative nature of this approach, FT analysis provides no physical insights. Other frameworks such as the Chebyshev stress decomposition and sequence of physical processes overcome this limitation. The Chebyshev stress decomposition method separates the overall stress into elastic and viscous components fitted by Chebyshev polynomials of the first kind, which are interrelated to Fourier coefficients. The Chebyshev polynomials are reduced to the following nonlinear measures [19]:

$$G'_M \equiv \frac{d\tau}{d\gamma} = \sum_{n:\text{odd}} nG'_n = e_1 - 3e_3 + \ldots, \tag{19.20}$$

$$G'_L \equiv \frac{\tau}{\gamma} = \sum_{n:odd} G'_n (-1)^{\frac{n-1}{2}} = e_1 + e_3 + \dots, \tag{19.21}$$

$$\eta'_M \equiv \frac{d\tau}{d\dot{\gamma}} = \frac{1}{\omega} \sum_{n:odd} n G''_n (-1)^{\frac{n-1}{2}} = v_1 - 3v_3 + \dots, \tag{19.22}$$

$$\eta'_L \equiv \frac{\tau}{\dot{\gamma}} = \frac{1}{\omega} \sum_{n:odd} G''_n = v_1 + v_3 + \dots, \tag{19.23}$$

where G'_M is the minimum-strain or tangent modulus at $\gamma(t) = 0$ and G'_L is the large-strain or secant modulus at $\gamma(t) = \gamma_{max}$. Likewise, h'_M is the minimum-rate viscosity and h'_L is the large-rate viscosity. The letters e_n and v_n refer to elastic and viscous Chebyshev coefficients of nth order fitting the data. All these material functions reduce to G' and G'' ($\eta' = G''/\omega$) in the LVR region. Comprehensive descriptions on the fundamentals and use of the Chebyshev polynomials framework are available in the literature [19, 22, 23]. Later, the "Sequence of Physical Processes" (SPP) method based on the Frenet-Serret theorem was developed [20]. This method has some important advantages over the Chebyshev decomposition approach because it describes the nonlinear moduli continuously in time and space rather than just in specific strain and strain rates of the oscillatory cycle. The Frenet-Serret theorem defines each point on the Lissajous curve by three vectors: one tangent to the response curve (T) (e.g., stress if strain is the independent excitation variable) one pointing to the center of the curve (N), and one being the cross product of the first two vectors (B). The projections of the binomial vectors (B) on the stress-strain curve define the transient elastic (G'_t) moduli, while its projection on the stress and strain rate curve defines the transient viscous (G''_t) moduli:

$$G'_t = -\frac{B_\gamma}{B_\sigma} = \frac{d\sigma}{d\gamma} \tag{19.24}$$

$$G''_t = -\frac{B_{\frac{\dot{\gamma}}{\omega}}}{B_\sigma} = \frac{d\sigma}{d\left(\frac{\dot{\gamma}}{\omega}\right)} \tag{19.25}$$

where B_γ, $B_{\dot{\gamma}/w}$, B_σ are the projections of binormal vector $B(t)$ along with the strain, strain rate, and stress axis, respectively. Plotting of the instantaneous G''_t versus G'_t plot (Cole-Cole plot) is a powerful way to evaluate the transient response of the material within an oscillation cycle. More details on the SPP approach can be found in the literature [20, 24].

Experiment LAOS Type and Data Collection

Major experimental considerations to keep in mind when performing LAOS experiments include selection of the most suitable experiment (i.e., LAOStrain vs. LAOStress), the form of data collection, rheometric artifacts prior to processing, and analysis of data. Due to the narrow linear viscoelastic regime of lipids and oleogels, careful handling of the sample is required to minimize disruption of the original network. This can be achieved by loading cylindrical pre-formed samples with controlled normal force, loading with geometries that minimize sample disturbance (e.g., vane) or by crystallization in-situ [18, 25]. Prior to data processing and analysis, it is important to be aware with possible artifacts arising during rheological and textural characterization as described in Sect. 19.4.

Selection of Experiment Type

The selection of LAOStrain versus LAOStress techniques and the measurement of corresponding material functions depend on three main factors: instrument specifications, material under investigation and its application, and structure-rheology models. Instrument specifications include rheometer design, performance, and sensitivity. Depending on the rheometer design, stress-control or strain-control may be more suitable one over the other. Additional intrinsic nonlinearities may arise such as for instruments that employ active deformation control to measure strain [26]. Microstructure "sensitivity" to deformation or loads also influences the selection of the protocol. For lipid-based materials and oleogels, LAOStrain allows better input control and deeper probing into the nonlinear regime than LAOStress that causes large strain jumps in the nonlinear region [27, 28]. Material application also defines properties of interest, e.g., butter, spreads, and shortenings undergo nonlinear shear rates during processing or usability, namely during lamination and spreading, and thus LAOStrain reflects better their use. Textural properties can also be described in terms of rheological material functions from LAOStrain with consistent measuring units in contrast to LAOStress [27]. Finally, selection of the input function also depends on the sensitivity of structure-rheology models to specific material functions, which help infer molecular-, nano-, or microscale structures [19].

Data Collection, Processing, and Analysis

LAOS requires acquiring raw oscillatory waveforms, which typically consists in collecting strain-stress raw signals using standard capabilities included in commercial rheometers software (e.g., TA Orchestrator software, Raw data LAOS waveform) [29, 30]. Beyond the LVR region, in the LAOStrain regime, the raw stress begins to show transient decays in amplitude. Any LAOS analysis using FT or stress decomposition Chebyshev representation incorporates periodic steady stress waveforms. Achievement of steady state flow can be verified by observing overlapping of the Lissajous-Bowditch loops, an equilibrium of the first-harmonic viscoelastic moduli G' and G'' or a plateau value of the shear stress over time (e.g., in a time sweep) at certain set of $\{\omega, \gamma_0\}$. In practice, however, a steady state may never be reached and hence, the number of applied cycles at a specific set of $\{\omega, \gamma_0\}$ is merely based on experimental observations. Data processing and analysis of LAOStrain is performed with a custom-written freeware MATLAB routine [31]. The software

requires time series signals of strain and stress along with user-specified parameters for analysis. Data processing of the signal requires inputting multiple steady oscillatory cycles to increase the signal to noise ratio. The software smooths the total stress signal by filtering out even and no-integer harmonics associated with random noise and broken shear symmetry. A cutoff frequency, typically $I_n/I_1 < 0.05$ are not considered, limits noise attributed to higher frequency components masking the real signal. The output of the software includes Fourier and Chebyshev spectrum of the stress response, intercycle, and intracycle viscoelastic material measures and time-series signals of elastic and viscous stresses, $\sigma^e(\gamma(t))$ and $\sigma^\epsilon(\dot{\gamma}(t))$, respectively [31]. A similar routine developed for LAOS analysis based on the sequence of physical processes is thoroughly described in Le et al. [32].

19.4   Experimental Artifacts

In general, rheological and textural measurements can be affected by several experimental artifacts, which "at best" change slightly the absolute values of material functions, and "at worst" communicate false mechanical behavior. For example, for cone penetrometry, samples need to be properly conditioned prior to experimentation and the use of standard methods such as those described by the American Oil Chemists' Society Cc1606 are encouraged to avoid arbitrary testing conditions. For compression tests, it is of upmost importance to prepare specimens as flat as possible due to their limited range of accuracy at $\lesssim 1\%$ which is within the yielding region of fats and oleogels. Buckling or bulging of the sample specimens and strong frictional effects at the boundaries are other artifacts that can emerge and be avoided by preparing adequate specimen sizes $h_0/D \sim 1$–1.5 and lubricated plates (e.g., coated with oil or Teflon) [12]. Treatises compiling experimental challenges to avoid "bad data" collection in shear rheology in soft materials are available in the literature [33, 34]. It is important that the practitioner is aware of these issues to mitigate/minimize their occurrence and select an appropriate experimental window during shear measurements. For lipids and oleogels, the most important sources of artifact include slip, edge fracture, and gap under-filling during "in situ" crystallization. Given the self-lubricated nature of lipids, it would be rather rare that slip does not occur. Key indications of slip include (1) "free motion" of the sample between the contacting boundaries and even migration outside the gap when slip is strongly present, (2) gap dependence of the apparent material response, (3) reduced flow stress, (4) irregular fluctuations in the transient response of the stress-strain signal in the Lissajous-Bowditch curves, (5) asymmetric and open intracycle Lissajous-Bowditch loops, (6) significant signal contribution from even harmonics $I_2/I_1 > 0.1$, and (7) secondary loops in Lissajous-Bowditch curves also indicate slip in some cases. Approaches to check for and minimize slip include looking for any of the signatures abovementioned, collecting data at different gaps, performing marker tests, testing rheological behavior with different measuring geometries, selecting an
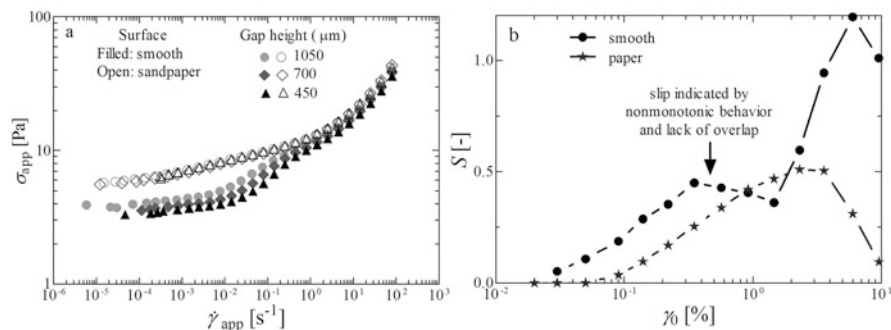
Fig. 19.6 (**a**) Wall slip on a smooth surface and elimination of wall slip on a sandpapered surface, respectively, for a water-in-oil emulsion (Nivea Lotion) tested using parallel plates of diameter $D = 40$ mm at multiple gaps $h = 450–1050$ mm. (Adapted from Ewoldt et al. [33]). (**b**) Wall slip and edge failure on smooth surface and absence of wall slip on a surface to which a cellulose filter paper has been attached, in a cake shortening using parallel plates of diameter $D = 20$ mm at a fixed gap $h = 1300$ mm and fixed frequency $\omega = 3.6$ rad/s. (Reproduced from [23], with permission from Taylor and Francis)

appropriate experimental window: define frequencies and amplitudes that prevent/ minimize slip, applying a normal force control: NFC $\approx$ 0–0.5 N during measurements to maximize sample-geometry contact during measurement and used of surfaces, e.g., sandblasted, crosshatched, that facilitate contact between the sample and measurement geometries. Edge failure is another potential artifact arising in stiff and brittle samples and can be detected by visual observation of the edge of the sample, marker tests, reduction in the apparent stress due to decrease in effective contact area, and gap dependence of the data. Sample under-filling occurs due to volume contraction upon crystallization or sol-to-gel transition in the rheometer and manifests as the development of a large negative normal force. Viable ways to eliminate underfilling include applying a zero normal force control or using internal gap adjustment procedures to compensate for sample contraction [35]. Overall, any of these artifacts can contribute to erroneous estimation of the viscoelastic moduli, waveforms distortion, and premature edge failure. Figure 19.6 illustrates examples where wall slip and edge failure manifest in a water-in oil emulsion and a cake shortening. In Fig. 19.6a, wall slip manifests as a lack of overlap of the material response as a function of gap height h, and a reduced stress response. In Fig. 19.6b, wall slip and edge failure cause premature yielding and a nonmonotonic behavior.

19.5 Case Studies: Bulk Fats, Oleogels, and Particle-Filled Gels

In the following sections, several case studies relevant to edible fats and oleogels are presented. In these, structure-rheology-texture relationships are established via rheology.

19.5.1 Fat Crystal Networks (Roll-In and All-Purpose Shortening)

A roll-in or laminating shortening is a soft fat material with high toughness. Toughness indicates the damage-tolerance of a material and quantifies its ability to dissipate energy under large loadings. A roll-in fat is used in the manufacture of croissants, Danish, and puff pastry where it enables uniform lamination, good gas retention, and lift volume, flakiness, and good mouthfeel [34]. During processing, a roll-in fat is extruded, squeezed, and shaped into micron-width films without breaking catastrophically. By contrast, an all-purpose shortening is used in multiple bakery applications mainly cake and icing but not in laminates, since it performs poorly. The baker is well familiar with this material performance and discriminates a "good" from a "bad" laminating fat by tactile perception. From scientific and health perspectives, it is desirable to pinpoint key rheological functions that describe the functionality of these materials as to enable inverse design of roll-in fats with no *trans* and lower saturates. Compression tests mimicking tactile perceptions were performed on each sample illustrate strikingly different macroscopic behavior (Fig. 19.7). On the one hand, a roll-in fat behaves as a ductile soft solid; on the other hand, an all-purpose fat behaves as a brittle soft solid material.

To elucidate material measures underlying the macroscopic behavior, LAOStrain deformations were applied, and stress responses analyzed and interpreted using Lissajous-Bowditch curves (not shown) and nonlinear measures (Fig. 19.7). In both material classes, linear viscoelasticity dominates the stress response at $\gamma_0 \approx 0.05\%$ (i.e., tight elliptical Lissajous-Bowditch loops). Above strains $\gamma_0 \approx 0.09\%$, Lissajous-Bowditch distort because of periodic nonlinear variations in the stress response particularly visible in local points of the stress response. In general, both samples display similar qualitative features, e.g., stress upturns at γ_0 (i.e., lower elasticity or energy storage at $\gamma = 0$ or $\dot{\gamma}_0$) in the elastic perspective and "bends" at $\dot{\gamma}_0$ (i.e., lower viscosity or energy dissipation at $\dot{\gamma} = 0$ or γ_0) in the viscous perspective indicating intracycle strain stiffening and intracycle shear thinning, respectively. At high strains $\gamma_0 \geq 6\%$, self-intersections and secondary loops occur at $\dot{\gamma}_0$ in the viscous curves attributed to stronger and quicker unloading of instantaneous elastic stresses, competition between network destruction and formation at high shear rates and even slippage [21]. Within an elastic LAOS cycle, e.g., at $\gamma_0 \approx 6\%$, the peak in stress demarks two regions: a nearly linear region preceding
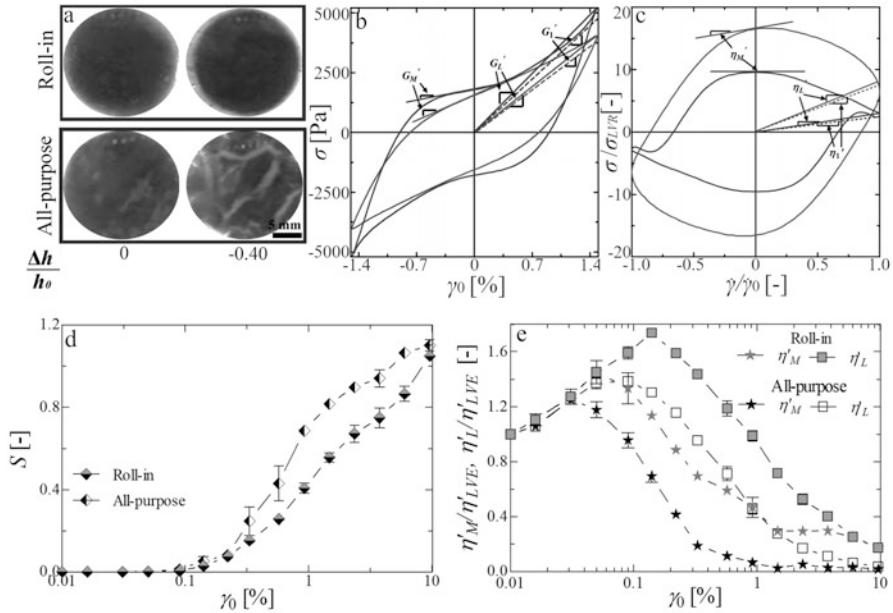
Fig. 19.7 (**a**) Views from below a transparent bottom plate supporting different mechanical behavior of fat shortenings. A roll-in shortening behaves as a ductile-like solid, whereas an all-purpose shortening resembles a brittle-like solid under compression. (**b**) Lissajous-Bowditch curve (elastic perspective) showing strain γ_0 versus stress σ for a selected data point $\gamma_0 = 1.47\%$, displaying graphical representation of local and global LAOS elastic measures: minimum-strain modulus G'_M, maximum-strain modulus G'_L, and average first-harmonic moduli G'_1 for fat shortenings. An all-purpose shortening displays more prominent stress upturns with higher stress maximum $\sigma \approx 5000$ Pa than a laminating shortening $\sigma \approx 4000$ Pa. (**c**) Lissajous-Bowditch curve (viscous perspective) showing shear rate normalized by shear rate input $\dot{\gamma}/\dot{\gamma}_0$ versus stress normalized by stress σ/σ_{LVR} within the LVR at $\gamma_0 = 0.01\%$. Curves are obtained from a selected strain input $\gamma_0 = 1.47\%$ ($\dot{\gamma}_0 = 0.05$ s^{-1}) and display graphical representation of local and global LAOS viscous measures: minimum-rate viscosity h'_M, maximum-rate viscosity h'_L, and average first-harmonic viscosity η'_1. An all-purpose shortening displays a Lissajous-Bowditch curve with stress upturns that enclose a smaller area than a roll-in shortening. Nonlinear local (**d**) elastic and (**e**) viscous measures for roll-in and all-purpose shortenings calculated from LAOS data at $\omega = 3.6$ rad/s. (d) Local elastic measures are integrated in the adimensional strain stiffening ratio $S = (G'_L - G'_M)/G'_L$. (**e**) Viscous measures are parametrized by the linear dynamic viscosity η'_{LVE} at $\gamma_0 = 0.01\%$. (Adapted and reproduced from [34], with permission from Springer)

the overshoot that extends roughly from the lower reversal point to the stress overshoot and a "flow" region following the overshoot. This linear stress region is associated with residual elasticities. In the "flow" region, as shear rate increases (or strain decreases), the stress decreases reaching a minimum. Subsequently, as the strain increases (or shear rate decreases), the stress increases again indicating thixotropy or network restructuring [18]. This progresses until the end of the half-cycle ($\gamma_0 = 0$ or $\dot{\gamma} = \dot{\gamma}_0$), and then the sequence is repeated during flow reversal.

Larger areas enclosed by the elastic Lissajous-Bowditch curves at high strains ($\gamma_0 \geq 6\%$), indicate increased plastic response, more evident in a roll-in shortening. Local LAOS measures indicate that a roll-in shortening and all-purpose store energy in a similar manner (i.e., comparable $S = (G'_L - G'_M)/G'_L$); however, they dissipate energy in a strikingly different way (i.e., different h'_M/η'_{LVE} and h'_L/η'_{LVE}). A roll-in shortening dissipates ~10× energy of an all-purpose shortening. To link the observed nonlinear mechanical response to nano-to-micro scale structures, ultra-small angle x-ray scattering was performed. Data fitted to the Unified Fit model revealed two major structural differences on: (1) the number of levels making up the fat hierarchy, (2) the morphology and size of nanoplatelets. A roll-in shortening had three structural levels, while an all-purpose shortening only two structural levels. A roll-in shortening had nanoplatelets characterized by "smooth" surfaces and average sizes about 10-fold smaller: ~50 nm, whereas an all-purpose shortening had nanoplatelets with "rough" surfaces and average size of ~500 nm. Based on rheology and the structural insight, it was suggested that a roll-in shortening dissipates more effectively shear deformations due to: (1) an "extra" hierarchical level that allows better energy allocation, (2) sliding of microscopic layer-like crystal aggregates in which the liquid oil could serve as a lubricant. Furthermore, the fact that several compositions share a unique rheological "fingerprint": increased viscous dissipation, indicates that the structure-function framework rather than exact bulk composition determines performance [34].

19.5.2 Particle-Filled Dispersions (High-Fat and Low-Fat Semi-Hard Cheeses and Spreads)

19.5.2.1 Soft Fillers: Viscoelastic Lipid Droplets Filling a Protein Matrix

From a material perspective, cheese can be considered an emulsion-filled gel. Rheology and texture are largely governed by the fat filler, its volume fraction, and its physicochemical properties: melting. Fat acts as a perfect filler as it tailors textural attributes such as firmness, springiness, rubberiness, and influences cheese processability. Any reformulation effort to produce low-fat cheese requires careful consideration of rheology and texture to anticipate quality and sensory trade-offs. In this case study, relationships between rheology and structure are presented for Gouda cheeses formulated with zero ($\phi_{fat} = 0$) and full fat content ($\phi_{fat} = 0.3$) [27]. By using LAOStrain, the effect of the fat filler on the "firm to fluid" or yielding transition of cheese is elucidated. Intercycle damage progression and failure of full-fat cheese differs from that of zero-fat cheese (Fig. 19.8). The roman numbers denote the various stages of stress response for both cheeses; I: elastic (i.e., linear grow-rate of the intercycle stress and recoverable strain), I-II: elastoviscoplastic (irrecoverable strain due to initiation of microcrack formation), II: global stress $\sigma'_{max}(\gamma_0)$ or elastic failure stress, III: decay of elastic stress (due to percolation of crack into larger fractures). The main differences are that a full-fat cheese shows larger initial
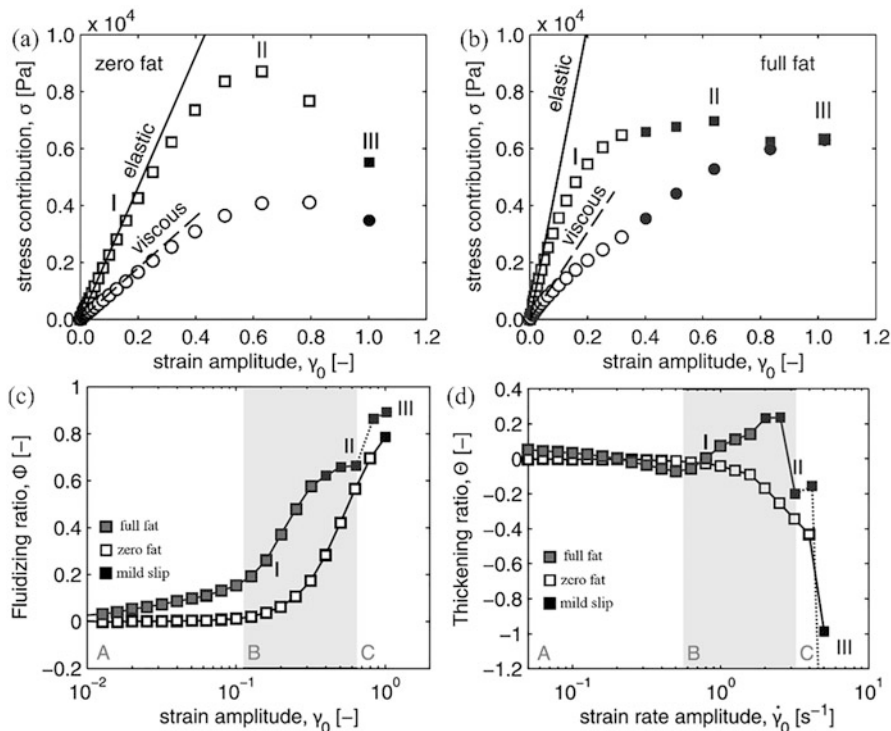
Fig. 19.8 Top panels (**a**, **b**): Evolution of the intracycle maxima of the elastic stress $\sigma'_{max}(\gamma_0)$ (hollow squares) and viscous stress $\sigma''_{max}(\gamma_0)$ (hollow circles) as a function of the strain amplitude γ_0 for (**a**) zero-fat and (**b**) full-fat cheese measured at $T = 25\,°C$ and a frequency $\omega = 5$ rad/s. The continuous and dashed lines represent the predictions of the linear viscoelastic constitutive model. Both zero-fat and full-fat cheese display an intercycle maximum of the elastic stress σ'_f (indicated by the numeral II) at a failure strain amplitude $\gamma_f \approx 0.7$. The intercycle maximum is defined as the failure criterion for the food gel. The full-fat cheese curve (**b**) displays a broad plateau in the maximum elastic stress σ'_{max} and a small decrease beyond the failure point. By contrast, the zero-fat cheese, shown in (**a**), displays a more clearly pronounced peak in the σ'_{max} max curve. The filled symbols indicate the strain amplitudes at which mild slip was observed. Bottom panels (**c**, **d**): Strain sweeps showing the evolution of (**c**) the fluidizing ratio ϕ and (**d**) the thickening ratio Θ, of zero-fat cheese and full-fat cheese measured at a temperature $T = 25\,°C$ and angular frequency $\omega = 5$ rad/s. (**c**) Both cheese formulations show comparable ultimate magnitudes of the fluidizing ratio; however, the rise of ϕ of full-fat cheese is more gradual and sets in at lower strains. (**d**) The non-Newtonian fluid properties of full-fat and zero-fat cheese are characterized by the evolution of the thickening ratio, which reveals three flow regimes A, B, and C. Zero-fat cheese displays continuous intercycle thinning, whereas full-fat cheese shows some initial thinning, followed by thickening and thinning. Beyond cycle II, the sample of full-fat cheese is no longer homogeneous, indicated with a dotted line in (**c**) and (**d**). The strain and strain-rate amplitudes at which mild slip is observed are indicated using filled symbols in each figure. (Reproduced from [27], with permission from Elsevier)

growth-rate (steeper slope) and larger elastoviscoplastic response (i.e., plastic response toward lower strain amplitudes I-II, and broad plateau prior to failure III) than a zero-fat cheese, since fat plasticizes the cheese matrix [27]. The maximum stress response $\sigma'_{\max}(\gamma_0)$ (its magnitude and rate of decline) is a strong indicator of "brittleness" (i.e., "the tendency to break under the condition of minimal previous plastic deformation"), a similar observation made in the first case study. To quantify these differences, Lissajous-Bowditch curves, and locally defined measures are inspected, the latter depicted in Fig. 19.8c, d.

Quantitatively, the local metrics G'_{M} and G'_{K} measure the onset of plastic flow and accumulation of damage in the elastic network and η'_{M} and η'_{L}, the associated viscous responses. The level of "fluidization" or the extent of "solid-to-fluid" transition in elastic and viscous perspectives are defined as:

$$\Phi \equiv \frac{G'_{\mathrm{K}} - G'_{\mathrm{M}}}{G'_{\mathrm{K}}} = \frac{12e_3 + 20e_5 + \dots}{e_1 + 9e_3 + 25e_5 + \dots} \quad \text{Elastic} \tag{19.26}$$

$$\Theta \equiv \frac{\eta'_{\mathrm{K}} - \eta'_{\mathrm{M}}}{\eta'_{\mathrm{K}}} = \frac{12v_3 + 20v_5 + \dots}{v_1 + 9v_3 + 25v_5 + \dots} \quad \text{Viscous} \tag{19.27}$$

These definitions are analogous to "stiffening" and "thickening" ratios described in Ewoldt et al. [30], with the only difference being that both G'_{K} and η'_{K} are tangential (not secant) measures to highlight modulus and viscosity at maximum strain/strain-rate, respectively [27, 30]. Figure 19.8c, d shows Φ and Θ for zero-fat and high-fat cheeses where three regimes are distinguished: (A) elastic response without plastic flow $\Theta \approx 0$ for zero-fat cheese versus initial elastic response followed by mild fluidization $\Phi > 0$ and thinning $\Theta < 0$ due to strain localization in the emulsified fat component, (B) start of fluidization/thinning $\Phi > 0$ and $\Theta > 0$ due to microcrack nucleation and propagation for zero-fat cheese versus continued fluidization $\Phi > 0$ and with shear "thickening" $\Theta > 0$ akin to rubber toughening for full-fat cheese, (C) extreme fluidization/thinning attributed to failure, which is driven by crack propagation and sample-spanning fractures for both zero-fat and high-fat cheeses.

A similar study for cheese spreads encompassing the interpretation of material responses based on the sequence of physical processes using the Frenet-Serret theorem was conducted [32]. In all cases, the Cole-Cole plots are positioned higher than the $G'_t = G''_t$ line, suggesting a predominant elastic behavior. In the linear viscoelastic region, the Cole-Cole plots appeared as very small deltoids between 0 and 4% strain. As the material enters the nonlinear region (>4%), the deltoids gradually increase in size due to material displacement and microstructural changes during an oscillatory cycle. In Fig. 19.9, the strain range between 10% and 50% induced the most displacement for both samples, although the deltoids of low-fat cheese spreads are bigger than those of high-fat cheese spreads within this strain range. These findings were qualitatively consistent with G'_{L} and G'_{M} obtained from
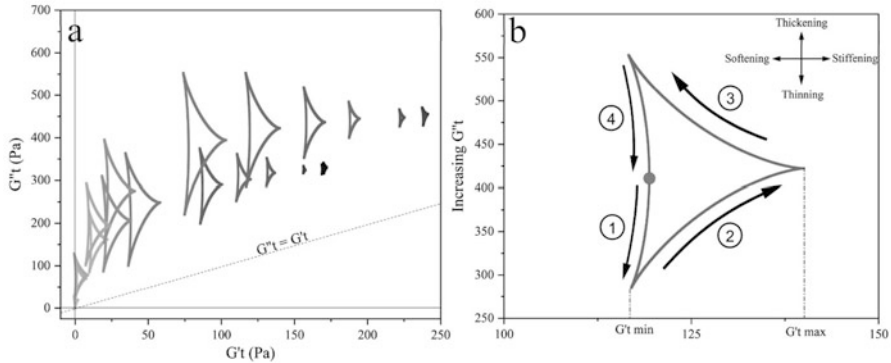
Fig. 19.9 (**a**) Cole-Cole plots of processed cheese spreads at increasing amplitudes. Low-fat cheese spreads lie higher than those of high-fat cheese spreads. (**b**) Zoom-in of a single Cole-Cole plot for a low-fat cheese spread demonstrating their general behavior during one oscillatory cycle. The dot denotes the starting point of the oscillatory cycle. (Reproduced from [32], with permission from Elsevier)

the Chebyshev decomposition method (not shown). Beyond 50% strain, the size of the deltoids in both samples decrease and become progressively comparable in size. This suggests that both cheeses have experienced similar irreversible network decay at higher deformations (80–1000%). Additionally, the shape of all deltoids for both cheeses experience a similar process of physical changes in each oscillatory cycle, described in 4 stages. These stages include (1) shear thinning and strain softening, (2) shear thickening and strain stiffening, (3) shear thickening and strain softening, (4) shear thinning and strain softening. These transitions coincided with those reported by Chebyshev parameters, with the additional transition from shear thinning (region 1) to shear thickening (stage 2) at the beginning of the oscillation cycle.

19.5.2.2 Hard Fillers: Rigid Particles Dispersed in a Lipid Gel Network

Many lipid-based suspensions such as chocolate, icing, and other confectionery contain rigid granular particles such as sugar and bulking agents, dispersed in a continuous phase. Filler addition is often sought to modulate stiffness, processability, and sensory perception. Successful replacement of the lipid phase by an oleogel phase requires partly that the suspensions exhibit similar rheological response. Recent studies suggest that in both cases, the mechanics of the composite material is akin to those hard fillers dispersed in a yield stress fluid. In what follows, the case of starch dispersed in a tripalmitin lipid gel network is presented. Starch particles were treated as noninteracting hard spheres based on preliminary findings. The elastic modulus, yield stress, and yield strain were described and interrelated through simple scaling laws from a micromechanical homogenization analysis of hard spheres isotropically distributed in yield stress fluids. For all models, the maximum packing fraction ϕ_m was equal to the random close packing of polydisperse hard
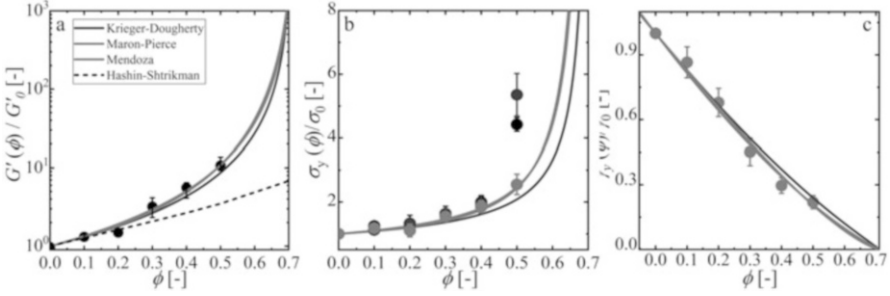
Fig. 19.10 Dimensionless rheological measures: (**a**) elastic modulus, (**b**) yield stress, and (**c**) yield strain, all as function of particle volume fraction, dispersed in a lipid gel. Experimental data is well described by empirical models: Krieger-Dougherty, Maron-Pierce, and Mendoza models, forced-fitted with a theoretical maximum packing volume fraction of 0.72 ± 0.01. (Reproduced from [36], with permission from Elsevier under the terms of the Creative Commons Attribution 4.0 International (CC BY 4.0) license)

sphere ϕ_{RCP} calculated based on a geometrical theory and using the log normal distribution of starch particles dispersed in oil as input. Figure 19.10 shows the dimensionless elastic moduli, yield stress, and yield strain as a function of volume fraction of starch. For all cases, the rheology is appropriately described using Krieger-Dougherty, Maron-Pierce, and Mendoza models derived from granular suspensions.

To illustrate, the forms of the Krieger Dougherty model for the elastic moduli, yield stress, and yield strain adequately described the rheology:

$$\frac{G'(\phi)}{G'_0} = \frac{1}{(1 - \phi/\phi_m)^{2.5\phi_m}} \tag{19.28}$$

$$\frac{\sigma_y(\phi)}{\sigma_0} = \sqrt{\frac{1 - \phi}{(1 - \phi/\phi_m)^{2.5\phi_m}}} \tag{19.29}$$

$$\frac{\gamma_y(\phi)}{\gamma_0} = \sqrt{(1 - \phi)(1 - \phi/\phi_m)^{2.5\phi}} \tag{19.30}$$

where G'_0, σ_0, and γ_0 are the plateau modulus, the yield stress, and the yield strain of the continuous lipid phase, respectively, and ϕ_m is the maximum volume packing. For the use and applicability of all models, readers are referred to the original study [36].

19.6   Conclusions

Rheological and mechanical measures encode key information about the static and dynamic mesostructures responsible for macroscopic performance, textural attributes, and processing of fats and oleogels. Several tests are available to probe the mechanics and rheology of fats and oleogels ranging from traditional and simple methods such as penetrometry to elaborate and advanced methods such as large amplitude oscillatory shear. Penetrometry tests can be useful to discriminate among different fat and oleogels. However, only controlled flows such as large amplitude oscillatory shear closely resemble nonlinear and transient flows encountered during processing and product use. By coupling large amplitude flows with other nonlinear flows such as extrusion-like flows, it is possible to access a broad map of viscoelasticity as a function of timescales and deformations. Such efforts will guide the inverse design and substitution of fats by oleogels. Connecting structure with rheology via phenomenological models and coupling rheology with structural probes can also iluminate the dynamic microscopic ensemble underlying the rheological response.

References

1. Szczesniak AS (2002) Texture is a sensory property. Food Qual 13:215–225. https://doi.org/10.1016/s0950-3293(01)00039-8
2. Wright AJ, Scanlon MG, Hartel RW, Marangoni AG (2008) Rheological properties of milkfat and butter. J Food Sci 66:1056–1071. https://doi.org/10.1111/j.1365-2621.2001.tb16082.x
3. Macias-Rodriguez BA, Marangoni AG (2020) Rheology and texture of cream, milk fat, butter and dairy fat spreads. In: Truong T, Lopez C, Bhandari B, Prakash S (eds) Dairy fat products and functionality: fundamental science and technology. Springer International Publishing, Cham, pp 245–275
4. Haighton AJ (1959) The measurement of the hardness of margarine and fats with cone penetrometers. J Am Oil Chem Soc 36:345–348. https://doi.org/10.1007/bf02640051
5. Hayakawa M, deMan JM (1982) Consistency of fractionated milk fat as measured by two penetration methods. J Dairy Sci 65:1095–1101. https://doi.org/10.3168/jds.S0022-0302(82)82317-5
6. Tanaka M, Man JMDE, Voisey PW (1971) Measurement of textural properties of foods with a constant speed cone penetrometer. J Texture Stud 2:306–315. https://doi.org/10.1111/j.1745-4603.1971.tb01007.x
7. Haighton AJ (1965) Worksoftening of margarine and shortening. J Am Oil Chem Soc 42:27–30. https://doi.org/10.1007/BF02558248
8. Shama F, Sherman P (1970) The influence of work softening on the viscoelastic properties of butter and margarine. J Texture Stud 1:196–205. https://doi.org/10.1111/j.1745-4603.1970.tb00723.x
9. Castro M, Giles DW, Macosko CW, Moaddel T (2010) Comparison of methods to measure yield stress of soft solids. J Rheol 54:81–94. https://doi.org/10.1122/1.3248001
10. Mishra K, Grob L, Kohler L, Zimmermann S, Gstöhl S, Fischer P, Windhab EJ (2021) Entrance flow of unfoamed and foamed Herschel–Bulkley fluids. J Rheol 65:1155–1168. https://doi.org/10.1122/8.0000286

11. Macosko CW (1994) Rheology: principles, measurements, and applications. Wiley-VCR, Hoboken
12. Kloek W, van Vliet T, Walstra P (2005) Mechanical properties of fat dispersions prepared in a mechanical crystallizer. J Texture Stud 36:544–568. https://doi.org/10.1111/j.1745-4603.2005.00031.x
13. Deman JM, Beers AM (1987) Fat crystal networks: structure and rheological properties. J Texture Stud 18:303–318. https://doi.org/10.1111/j.1745-4603.1987.tb00908.x
14. Coussot P, Tabuteau H, Chateau X, Tocquer L, Ovarlez G (2006) Aging and solid or liquid behavior in pastes. J Rheol 50:975–994. https://doi.org/10.1122/1.2337259
15. Dinkgreve M, Paredes J, Denn MM, Bonn D (2016) On different ways of measuring "the" yield stress. J Nonnewton Fluid Mech 238:233–241. https://doi.org/10.1016/j.jnnfm.2016.11.001
16. Van den Tempel M (1961) Mechanical properties of plastic-disperse systems at very small deformations. J Colloid Sci 16:284–296. https://doi.org/10.1016/0095-8522(61)90005-8
17. Narine SS, Marangoni AG (1999) Mechanical and structural model of fractal networks of fat crystals at low deformations. Phys Rev E 60:6991–7000. https://doi.org/10.1103/physreve.60.6991
18. Macias-Rodriguez B, Marangoni AG (2016) Rheological characterization of triglyceride short-enings. Rheol Acta 1–13. https://doi.org/10.1007/s00397-016-0951-6
19. Ewoldt RH, Bharadwaj NA (2013) Low-dimensional intrinsic material functions for nonlinear viscoelasticity. Rheol Acta 52:201–219. https://doi.org/10.1007/s00397-013-0686-6
20. Rogers SA (2012) A sequence of physical processes determined and quantified in Laos: an instantaneous local 2d/3d approach. J Rheol 56:1129–1151. https://doi.org/10.1122/1.4726083
21. Ewoldt RH, McKinley GH (2010) On secondary loops in Laos via self-intersection of lissajous–bowditch curves. Rheol Acta 49:213–219. https://doi.org/10.1007/s00397-009-0408-2
22. Macias Rodriguez BA (2019) Nonlinear rheology of fats using large amplitude oscillatory shear tests. In: Marangoni AG (ed) Structure-function analysis of edible fats, 12th edn. AOCS Press, pp 169–195
23. Macias-Rodriguez BA, Marangoni AA (2018) Linear and nonlinear rheological behavior of fat crystal networks. Crit Rev Food Sci Nutr 58:2398–2415. https://doi.org/10.1080/10408398.2017.1325835
24. Rogers SA, Lettinga MP (2012) A sequence of physical processes determined and quantified in large-amplitude oscillatory shear (Laos): application to theoretical nonlinear models. J Rheol 56:1–25. https://doi.org/10.1122/1.3662962
25. Thareja P, Street CB, Wagner NJ, Vethamuthu MS, Hermanson KD, Ananthapadmanabhan KP (2011) Development of an in situ rheological method to characterize fatty acid crystallization in complex fluids. Colloids Surf A Physicochem Eng Asp 388:12–20. https://doi.org/10.1016/j.colsurfa.2011.07.038
26. Merger D, Wilhelm M (2014) Intrinsic nonlinearity from laostrain—experiments on various strain- and stress-controlled rheometers: a quantitative comparison. Rheol Acta 53:621–634. https://doi.org/10.1007/s00397-014-0781-3
27. Faber TJ, Van Breemen LCA, McKinley GH (2017) From firm to fluid – structure-texture relations of filled gels probed under large amplitude oscillatory shear. J Food Eng 210:1–18. https://doi.org/10.1016/j.jfoodeng.2017.03.028
28. Ramamirtham S, Shahin A, Basavaraj MG, Deshpande AP (2017) Controlling the yield behavior of fat-oil mixtures using cooling rate. Rheol Acta 56:971–982. https://doi.org/10.1007/s00397-017-1048-6
29. Läuger J, Stettin H (2010) Differences between stress and strain control in the non-linear behavior of complex fluids. Rheol Acta 49:909–930. https://doi.org/10.1007/s00397-010-0450-0
30. Ewoldt RH, Hosoi AE, McKinley GH (2008) New measures for characterizing nonlinear viscoelasticity in large amplitude oscillatory shear. J Rheol 52:1427–1458. https://doi.org/10.1122/1.2970095

31. Ewoldt RH, Hosoi AE, McKinley GH (2009) Nonlinear viscoelastic biomaterials: meaningful characterization and engineering inspiration. Integr Comp Biol 49:40–50. https://doi.org/10.1093/icb/icp010

32. Le AM, Erturk MY, Kokini J (2023) Effect of fat on non-linear rheological behavior of processed cheese spreads using coupled amplitude-frequency sweeps, fourier transform-chebyshev polynomials method, sequence of physical processes, and quantitative network analysis. J Food Eng 336:111193. https://doi.org/10.1016/j.jfoodeng.2022.111193

33. Ewoldt RH, Johnston MT, Caretta LM (2015) Experimental challenges of shear rheology: how to avoid bad data. In: Spagnolie SE (ed) Complex fluids in biological systems: experiment, theory, and computation. Springer, New York, pp 207–241

34. Macias-Rodriguez BA, Ewoldt RH, Marangoni AG (2018) Nonlinear viscoelasticity of fat crystal networks. Rheol Acta 57:251–266. https://doi.org/10.1007/s00397-018-1072-1

35. Mao B, Divoux T, Snabre P (2016) Normal force controlled rheology applied to agar gelation. J Rheol 60:473–489. https://doi.org/10.1122/1.4944994

36. Macias-Rodriguez BA, Velikov KP (2022) Elastic reinforcement and yielding of starch-filled lipid gels. Food Struct 32:100257. https://doi.org/10.1016/j.foostr.2022.100257